Biomimetic Superhydrophobic Surfaces by Nanoarchitectonics with Natural Sunflower Pollen

Jian Li, Jingyu Deng, Chenchen Zhou, Jueying Yang, Sungmin Shin, Bernard P. Binks, and Nam-Joon Cho*

Superhydrophobic surfaces, known for their water-repellent, and self-cleaning properties, are widely used in various applications. These advanced functional surfaces exhibit high contact angles (>150°), achieved through low surface energy chemistries and hierarchical roughness. Natural sunflower pollen is micron-sized spherical particles with nano-sized spikes on the surface. This study engineered superhydrophobic coatings using the unique hierarchical structure of sunflower pollen and low surface energy additives like polydimethylsiloxane (PDMS) and silane additives such as 1H,1H,2H,2H-perfluorooctyltrichlorosilane (FTS), octadecyltrichlorosilane (OTS) and dichlorodimethylsilane (DCDMS). The pollen content significantly modulates surface structure, roughness, and water contact angle. Higher pollen content enhances roughness and water repellency by creating micro-nano hierarchical structures. Pollen-PDMS-FTS and Pollen-PDMS coatings demonstrated the highest water contact angles (165 ± 2° and 163 ± 3°, respectively) and lowest sliding angles (4.5 ± 1° and 7.6 ± 2.6°, respectively), achieving a "lotus effect." Conversely, Pollen-PDMS-OTS or Pollen-PDMS-DCDMS coatings resulted in high sliding angles and water adhesion, producing a "rose petal effect." These "lotus effect" coatings are effectively applied in self-cleaning and water displacement in oil pipelines on hilly terrain. This study provides insights into the interplay between hierarchical structure and surface-free energy for designing superhydrophobic surfaces tailored for specific applications.

J. Li, J. Deng, C. Zhou, J. Yang, S. Shin, N.-J. Cho
School of Materials Science and Engineering
Nanyang Technological University
50 Nanyang Avenue, Singapore 639798, Singapore
E-mail: njcho@ntu.edu.sg
J. Li, J. Deng, C. Zhou, J. Yang, S. Shin, N.-J. Cho
Centre for Cross Economy
Nanyang Technological University
50 Nanyang Avenue, Singapore 639798, Singapore
B. P. Binks
Department of Chemistry
University of Hull
Hull HU6 7RX, UK

1. Introduction

Superhydrophobic surfaces, characterized by an air–water contact angle (WCA, θ_w) exceeding 150° exhibit remarkable resistance to wetting. In nature, numerous examples of superhydrophobic surfaces are found in plants and animals, such as lotus (*Nelumbo nucifera*) leaves,[1] colocasia esculenta leaves,[2] rose petals,[3] butterfly wings, fly eyes, gecko feet, water strider legs, etc.[4] Drawing inspiration from these natural surfaces, researchers have developed artificial superhydrophobic surfaces for various applications in daily life and industry, including self-cleaning,[5] anti-contamination,[6] oil–water separation,[7] heat transfer,[8] anti-fogging,[9] anti-icing/de-icing,[10] adhesion and drag reduction,[11] anti-fouling/anti-biofouling,[12] anti-bacterial surfaces,[13] anti-corrosion,[14] solar-driven interfacial evaporation.[15] The wetting behavior of liquid droplets on solid surfaces depends on surface chemistry and roughness.[16] On a flat surface with low surface energy, the maximum WCA achievable by a water droplet is ≈120°.[17] In order to achieve superhydrophobic surfaces with WCA > 150°, the surface requires a hierarchical roughness with micro/nanoscale structures beside coatings of low surface energy.[16c,18] Lotus leaves, for instance, possess a water-repellent surface due to their hierarchical micro-/nanostructure and low surface energy, enabling water droplets to roll off easily without any liquid adhering, thus exhibiting self-cleaning capabilities.[1,2,19] Conversely, rose petals exhibit super-hydrophobicity but high water adhesion, resulting in water droplets unable to roll off the petal surface even when the petals are turned upside down.[3] Known from nature, these superhydrophobic surfaces are categorized into the "lotus effect" with low water adhesion and the "rose petal effect" with high adhesion. Wetting on smooth solid surfaces can be described by Young's equation, while rough surfaces are analyzed using the Wenzel model. Notably, water droplets on the "lotus leaf effect" surface adopt the Cassie–Baxter state, whereas those on the "rose petal effect" surface assume the impregnating Cassie–Baxter state.[3] Inspired by this principle, superhydrophobic surfaces have been developed through the creation of diverse micro/nanostructures with varying

**ADVANCED
SCIENCE NEWS**

www.advancedsciencenews.com

**NANO · MICRO
small**

www.small-journal.com

roughness and alterations in surface chemistry. The most prevalent approaches involve modifying surface roughness using a range of techniques, including sol–gel coating processes,[14a,20] emulsion polymerization,[21] wet etching and liquid phase deposition, chemical vapor deposition,[22] self-assembly,[23] colloidal templating,[24] electrospinning,[7c,25] lithography,[26] layer-by-layer assembly,[12c,13a] etc.

In alignment with the United Nations Sustainable Development Goals aimed at fostering a more sustainable future, we need to develop cross economy by leveraging natural materials efficiently.[27] By innovating new functionalities for these materials, we can alleviate environmental burdens significantly. Pollen, a microscopic particle produced by plants during reproduction, serves to encapsulate and convey the male genetic material in flowering plants to fulfil their reproductive requirements. To ensure successful reproduction, plants produce substantial quantities of pollen, a significant portion of which becomes "bio-waste" and is readily available in abundance at low cost. As a versatile and abundant natural material, pollen has many potential applications, including as a drug delivery vehicle, microcapsules for drug delivery, pollen paper, micromotors/microbots, etc.[28] Recent studies have also tentatively explored the utilization of pollen and spores in creating superhydrophobic surfaces.[29] Hou et al. investigated papillae-enhanced hydrophobicity of polytetrafluoroethylene-polyphenylene sulfite films with rape pollen, achieving a superhydrophobic surface with a water contact angle of 151.5° and sliding angle of 4° by adjusting papillae density.[29a] Additionally, lycopodium spores have created "rose petal effect" surfaces with high apparent contact angles and strong adhesion of water droplets.[29b]

In nature, pollen of various plants exhibit diverse size, shape, and surface morphology with common size variations ranging from 2 to 250 μm and displaying excellent size uniformity within the same species.[30] Among these, natural sunflower pollen has a unique spherical microstructure with a uniform diameter of ≈30 μm, featuring a porous surface decorated with evenly distributed nano-sized spikes.[28a,31] The well-known superhydrophobic surface of lotus leaves arises from its hierarchical structure, comprising micron-sized papillae and nano-sized wax tubules.[2,19] Sunflower pollen shares a similar hierarchical micro/nanoscale structure. Therefore, we hypothesize that sunflower pollen grains could serve as a basis for developing superhydrophobic surfaces due to their micron-sized spherical particles overgrown with nanoscale spikes.

We created these superhydrophobic surfaces by applying a hybrid coating. The coating consists of polydimethylsiloxane (PDMS) combined with either natural or silane-modified sunflower pollen, with the silanes used being 1H,1H,2H,2H-perfluorooctyl-trichlorosilane (FTS), octadecyltrichlorosilane (OTS) or dichlorodimethylsilane (DCDMS), respectively. We anticipate that the superhydrophobic surfaces will feature the hierarchical micro/nanoscale roughness imparted by sunflower pollen. The combination of PDMS and the silane additives will furnish the surfaces with a hydrophobic chemical composition characterized by low surface energy.

We investigate the impact of pollen content in the coating on surface roughness (R_a) and structure. Additionally, we study how surface energy, surface roughness, and structure affect surface wettability including WCA, sliding angle of water droplets (WSA), contact angle hysteresis (CAH), and water adhesion. We further explore the transition mechanism from the "Lotus effect" to the "rose petal effect" superhydrophobic surfaces by exploring the relationship between surface morphology and surface energy. Finally, we investigate the efficacy of the "Lotus effect" superhydrophobic coating for water displacement in pipelines situated in hilly terrains as well as its self-cleaning ability.
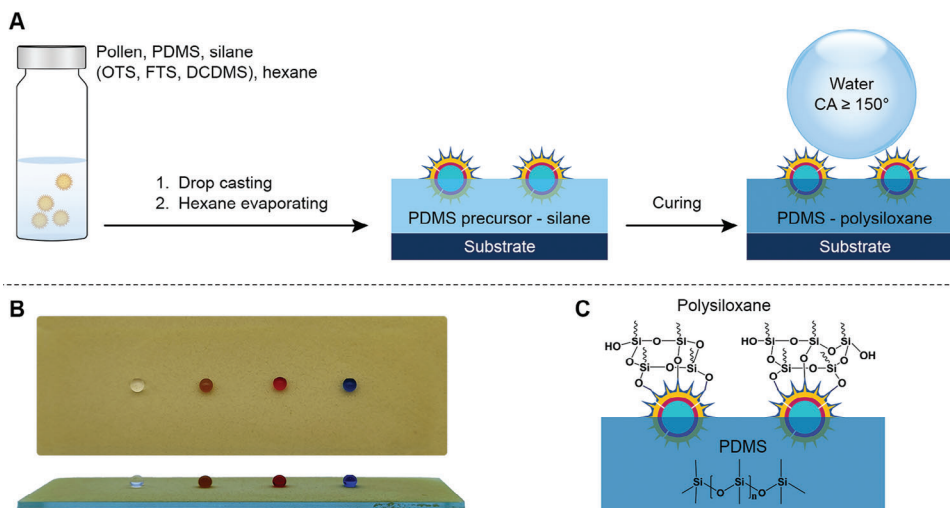
2. Results and Discussion

2.1. Fabrication of Superhydrophobic Surfaces

To create superhydrophobic surfaces, we utilize natural sunflower pollen beginning with the collection of pollen grains from the sunflower plant of the *Helianthus annuus* species (**Figure 1**). These pollen grains possess a hollow microcapsule structure with a two-layered wall and apertures, and the entire grain surface is covered in lipidic cement.[32] This lipidic cement was removed through a defatting process involving sequential rinsing with water, acetone and diethyl ether.[32,33] Following the removal of the lipid cement, defatted sunflower pollen exhibits a spiky structure on its surface. The bar chart inset in the Scanning electron microscopy (SEM) image of Figure 1 displays the size distribution of the defatted sunflower pollen. The dry defatted pollen has a diameter of 33.5 ± 1.1 μm, with spike lengths of 5.8 ± 0.8 μm. The defatted sunflower pollen was then used to fabricate superhydrophobic surfaces. The defatted pollen and PDMS precursor with/without a silane additive (FTS, OTS, or DCDMS, respectively) were uniformly mixed in hexane, drop-cast onto glass substrates or plastic dishes, dried, and left at room temperature for over five days to allow the PDMS and silane additives to crosslink and solidify, effectively coating the sunflower pollen surface (**Figure 2A**). As a result, the cured coating made of sunflower pollen, PDMS, and polysiloxane exhibited a superhydrophobic surface when exposed to pure water, yellow tea water, red dye
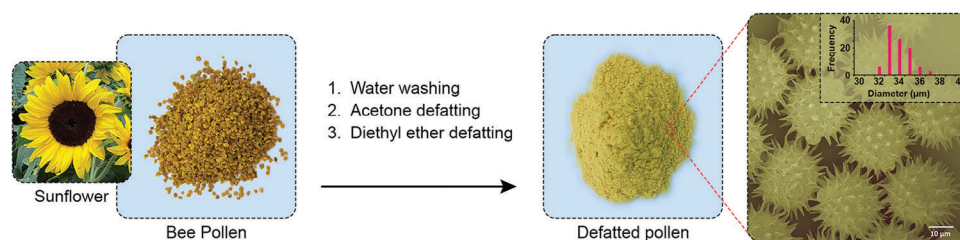
Figure 1. Schematic diagram of the process for preparing defatted sunflower pollen from bee pollen collected by bees from sunflower plants. Far right: SEM image of dried defatted sunflower pollen with (inset) particle size distribution.

**ADVANCED
SCIENCE NEWS**

www.advancedsciencenews.com

NANO · MICRO
small

www.small-journal.com

Figure 2. (A) Schematic diagram of the process for preparing superhydrophobic surfaces based on defatted sunflower pollen. (B) Top–down and side view photographs of polar liquid droplets (from left to right: pure water, yellow tea water, red dyed water, blue dyed water) sitting on the P-PDMS-FTS superhydrophobic surface. (C) Schematic illustration of P-PDMS-silane coating surface.

water, and blue dye water (Figure 2B), with a thickness of hundreds of microns (Figure S1, Supporting Information). The pollen surface features a dual-network coating: one composed of a cross-linked PDMS network, and another polysiloxane network formed by silane reacting with —OH groups present on the pollen surfaces, followed by hydrolysis and self-condensation (Figure 2C).
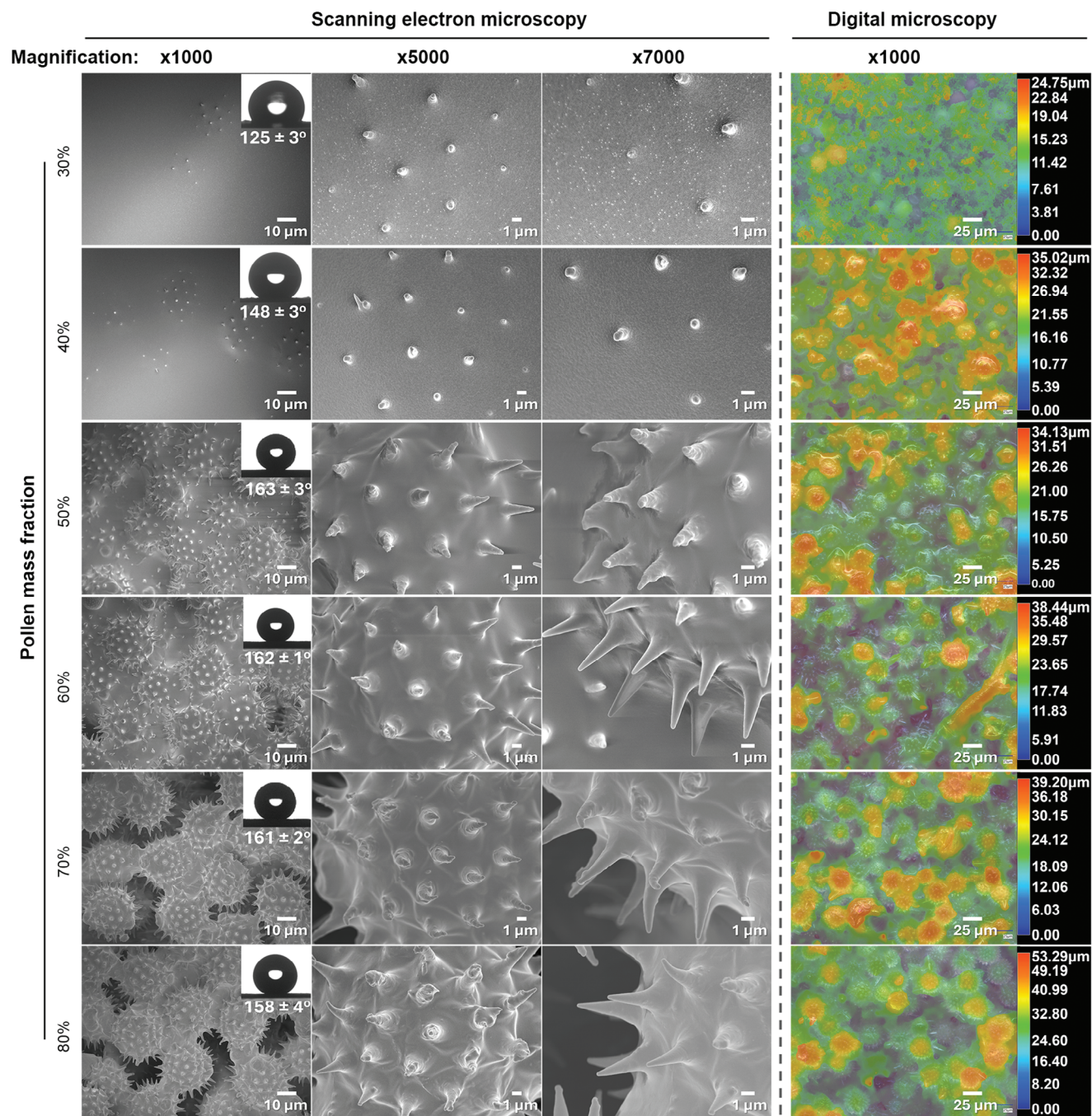
2.2. Morphology and Super-Hydrophobicity of Coatings

The SEM and digital microscopy images depict the surface morphology of pollen-PDMS (P-PDMS) coatings (**Figure 3**; Figure S2, Supporting Information) and pollen-PDMS-FTS (P-PDMS-FTS) coatings (Figure S3, Supporting Information) with varying mass fraction of sunflower pollen (f_{pollen}). As f_{pollen} is below 40%, almost all pollen grains are encapsulated within the PDMS matrix. Only the topmost pollen grains showed conical nanostructure protruding from certain spike terminal parts without revealing the microstructure of the entire micron-sized pollen. As f_{pollen} exceeds 40%, the coating surface gradually develops a heterogeneous micro/nano double-layer structure, like the surface of a lotus leaf.[1,19] This occurs because PDMS progressively fails to fill the gaps between pollen grains allowing the surface spikes of the uppermost pollen grains to become more exposed until the entire pollen structures are fully exposed. The Ra values of all coatings were measured from 3D depth composition images obtained by digital microscopy, as shown in Figure 3 and Figure S3 (Supporting Information). Clearly, greater Ra was observed with increasing pollen content in the coating (**Figure 4A**), which can be attributed to the exposure of pollen body shape. There was no significant difference in the Ra values among all types of coatings with the same f_{pollen}. However, the Ra values in all coatings with f_{pollen} = 30% are significantly lower than those in all coatings with f_{pollen} ≥40%. For P-PDMS coating, the Ra values at f_{pollen} = 40% are significantly lower than those at f_{pollen} = 50%, whereas for all other types of coatings, the Ra values show no significant difference between f_{pollen} = 40% and f_{pollen} = 50%. When f_{pollen}

exceeds 50%, the Ra value in every type of coatings reaches its maximum and exhibits no significant change thereafter. There was no significant difference in the Ra values of all coatings with f_{pollen} = 50–80%. All these variations in Ra correspond to changes in the surface morphology of the coatings with varying pollen content, as depicted in Figure 3 and Figure S3 (Supporting Information). The surface morphology, characterized by micro-/nanostructures and increased roughness induced by sunflower pollen, combined with the low surface free energy chemistry provided by PDMS and silane additives, is essential in ensuring the super-hydrophobicity of the coating surface. Then the surface wettability including WCA, WSA, and CAH was investigated. Among them, WCA characterizes the superhydrophobic property of the coating surface while WSA and CAH evaluate water adhesion on the coating surface.

Figure 4B shows the air–water contact angle on the surfaces of different coatings, including P-PDMS, P-PDMS-FTS, pollen-PDMS-OTS (P-PDMS-OTS), and pollen-PDMS-DCDMS (P-PDMS-DCDMS), with varying pollen content. Among all P-PDMS-FTS coatings, the mass ratio of PDMS to FTS was set at 8:2, as this ratio provided the best performance (Figure S4, Supporting Information). Consequently, the same mass ratio of PDMS to silane was consistently maintained for all other coatings. The contact angle increases with pollen content reaching maximum values for P-PDMS, P-PDMS-FTS, and P-PDMS-OTS coatings when f_{pollen} is between 50% and 70%. This trend is consistent with changes in Ra and structure. When f_{pollen} is less than 40%, the apparent contact angle θ_w is below 150°, necessitating description using the Wenzel model:[16b] $\cos \theta_w = r \cos \theta_Y$, where θ_Y is Young's contact angle of a liquid on an ideal flat and smooth solid surface, and r is the roughness ratio defined as the ratio between the actual and projected solid surface area ($r = 1$ for a smooth surface and > 1 for a rough surface). Figure 4C shows the roughness ratio r of P-PDMS-FTS and P-PDMS surfaces calculated using the equation: $r = 1 + \frac{\frac{1}{4}\pi D^2 (\csc \frac{\alpha}{2} - 1)}{p^2}$, with all the parameters obtained from the SEM images in Figure 3 and Figure S3 (Supporting Information). Figure 4D displays a schematic

**ADVANCED
SCIENCE NEWS**
www.advancedsciencenews.com

**NANO · MICRO
small**
www.small-journal.com

Figure 3. SEM and digital microscopy images of P-PDMS coating surfaces with a pollen mass fraction of 30% to 80%. Inset: Side view photograph of a water droplet in air on the respective surface along with the corresponding contact angle. The digital microscopy image displays a color map of the coating surface with the color bar indicating height in µm.

diagram of the exposed spike structure and dimensions on the coating. As the pollen content increases, the roughness ratio r rises from 1.06 to ≈1.77, mirroring the trends in Ra (Figure 4A) and contact angle (Figure 4B). On the superhydrophobic surface with $\theta_w > 150°$, the apparent water contact angle should be described by the Cassie–Baxter formula:[16c] $\cos \theta_w = f_1 \cos \theta_Y - f_2$, where f_1 is the area fraction of the solid surface wet by the liquid, and f_2 is the area fraction of the liquid–air interface under

the droplet. Here, $f_1 = \frac{\frac{1}{2}\pi d_1^2}{p^2}$ and $f_2 \approx 1 - \frac{\frac{1}{4}\pi d_1^2}{p^2}$. The parameter f_1, determined by the end area of the exposed spike, consistently remains relatively low, typically ranging between 0.5% and 4%, as shown in Figure 4E. Additionally, the increase in f_{pollen} leads to more cavities between pollen grains, thus forming more air pockets, as illustrated in SEM images in Figure 3 and Figure S3 (Supporting Information). These air pockets reduce the contact

ADVANCED
SCIENCE NEWS

www.advancedsciencenews.com

NANO · MICRO
small
www.small-journal.com
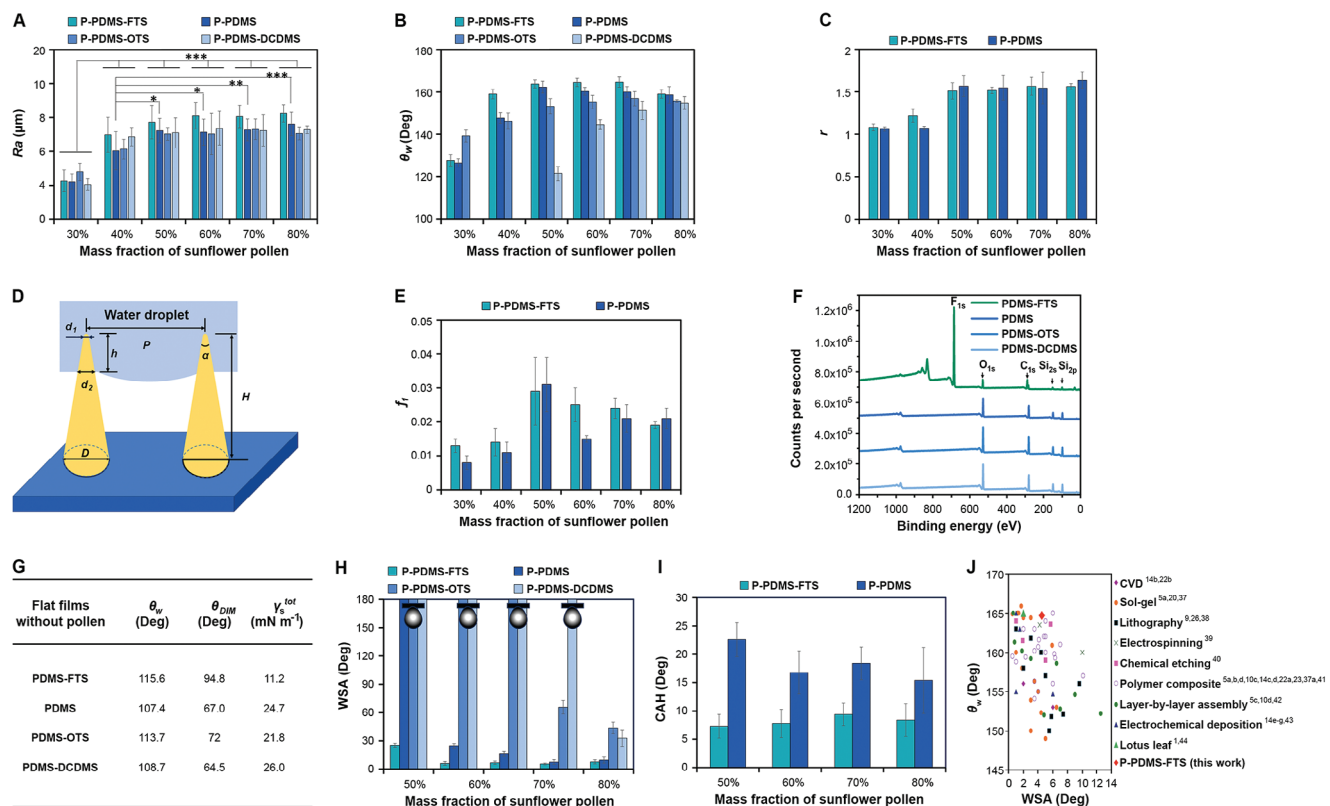
Figure 4. (A) Ra ($n = 10$) and (B) θ_w ($n = 10$) of P-PDMS-FTS, P-PDMS, P-PDMS-OTS and P-PDMS-DCDMS coatings with different mass fractions of sunflower pollen. (C) Roughness ratio r ($n = 10$) in the Wenzel equation which is derived from SEM images in Figure 3 and Figure S3 (Supporting Information). (D) Parameters of spikes on the coating surface which are used to describe the roughness ratio and parameter f_1. (E) Parameter f_1 ($n = 10$) in the Cassie-Baxter equation which is derived from SEM images in Figure 3 and Figure S3 (Supporting Information). (F) XPS of P-PDMS-FTS, P-PDMS, P-PDMS-OTS and P-PDMS-DCDMS coatings. (G) Air–water and air-diiodomethane (θ_{DIM}) contact angles and surface energy of PDMS-FTS, PDMS, PDMS-OTS and PDMS-DCDMS matrices without pollen. (H) Sliding angle of water droplet in air on P-PDMS-FTS, P-PDMS, P-PDMS-OTS and P-PDMS-DCDMS surfaces. The inset diagram shows that a drop of water can hang upside down at 180° on the corresponding surface. (I) CAH ($n = 10$) of water droplets on P-PDMS-FTS and P-PDMS surfaces with different mass fraction of sunflower pollen. (J) Air–water contact angle versus WSA for this work and literature work.[1,5,9,10,14,20,22,23,26,37-43] * $p \le 0.05$, ** $p \le 0.01$, and *** $p \le 0.001$.

area between the water droplet and the solid surface, thereby increasing the contact angle and facilitating the development of superhydrophobic surfaces. When f_{pollen} is 50–70%, θ_w reaches a maximum due to the maximum Ra, f_1 and air pockets.

In addition to Ra and surface structure, surface chemistry plays a crucial role in determining surface wettability. To achieve low surface energy, PDMS, PDMS-FTS, PDMS-OTS, and PDMS-DCDMS are incorporated into the coating matrix. These materials provide different surface energies due to variations in their carbon chain lengths and elemental compositions along their chains. Figure 4F shows X-ray photoelectron spectroscopy (XPS) spectra of P-PDMS, P-PDMS-FTS, P-PDMS-OTS, and P-PDMS-DCDMS coatings. The binding energies of F_{1s}, O_{1s}, C_{1s}, and Si_{2p} are at 687.0, 531.0, 289.0 and 101.0 eV, respectively. The Fourier transform infrared spectroscopy (FTIR) spectra in Figure S5 (Supporting Information) provide further insights into the chemical structure of the coatings. The characteristic absorption peaks at 2960, 2926, and 2856 cm^{-1} correspond to C—H stretching, while the peak at 1461 cm^{-1} is attributed to C-H bending. Peaks at 1092, 1021, and 801 cm^{-1} are linked to C—O/Si—O—Si/Si—O—C stretching, C—O stretching, and Si—O—Si stretching, respectively. In the P-PDMS-FTS

sample, characteristic absorption peaks related to C-F stretching are observed at 1378 and 1198 cm^{-1}. The XPS and FTIR patterns show that the P-PDMS-FTS coating has rich fluorine element on the surface due to FTS. The table in Figure 4G demonstrates that the flat and smooth surfaces of PDMS, PDMS-FTS, PDMS-OTS, and PDMS-DCDMS films without pollen have air–water contact angles (θ_Y) ranging from 107.4° to 115.6°, which are much smaller than all the coating surfaces with f_{pollen} ranging from 30% to 80%. These PDMS, PDMS-FTS, PDMS-OTS, and PDMS-DCDMS films exhibit low surface energies, ranging from 11.2 to 26.0 mN m^{-1}. Among them, PDMS-FTS has the lowest surface energy while PDMS-DCDMS has the highest. Consequently, the P-PDMS-FTS coating has the largest θ_w, followed by P-PDMS and P-PDMS-OTS, whereas the P-PDMS-DCDMS coating has the smallest θ_w, despite the four types of coating sharing the same surface structure and roughness. Therefore, considering the aforementioned data, coatings based on sunflower pollen exhibit high roughness, low f_1 and low surface energy, all of which contribute to the formation of superhydrophobic surfaces.

The WSA and CAH were also measured to assess surface heterogeneity and water adhesion, as depicted in Figure 4H,I, and Figure S6 (Supporting Information). When the pollen content
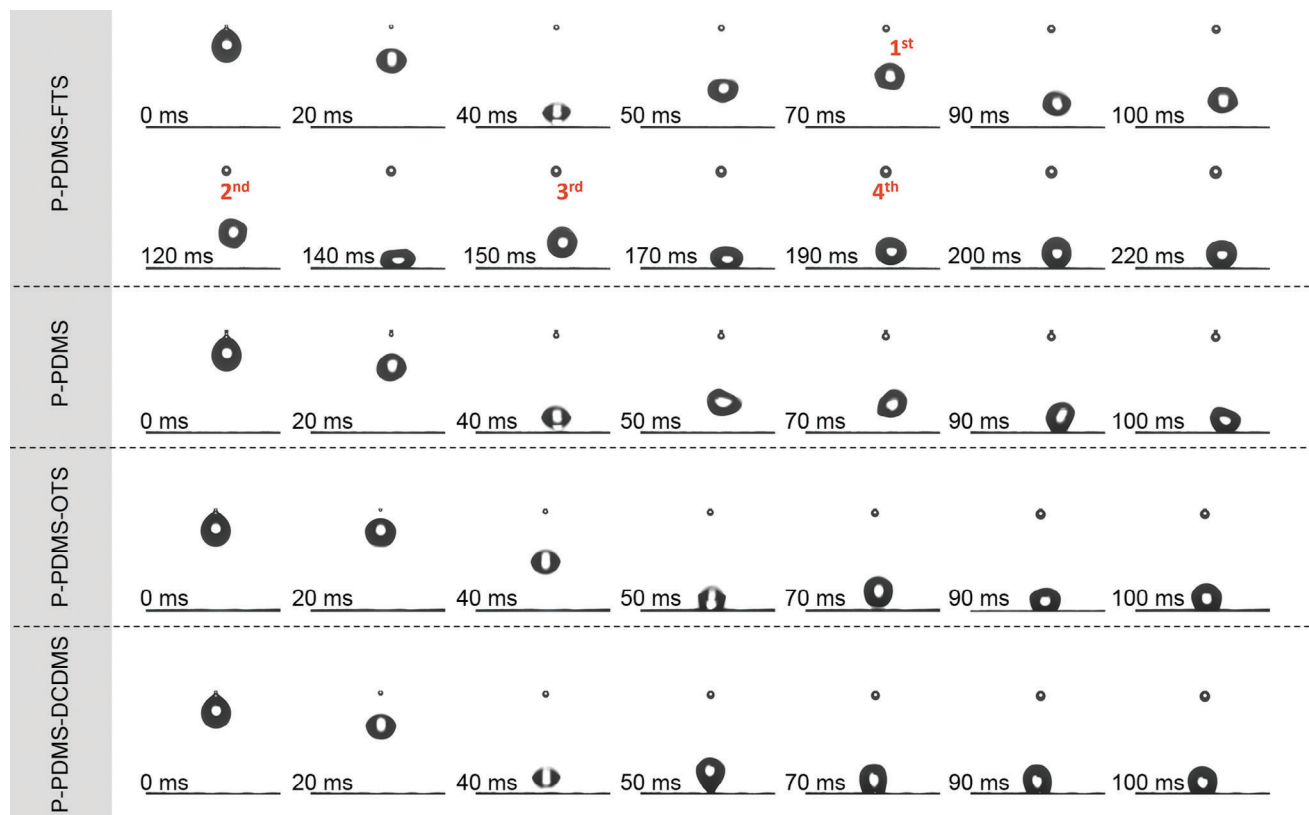
Figure 5. Water droplets bouncing on various coated surfaces: P-PDMS-FTS, P-PDMS, P-PDMS-OTS and P-PDMS-DCDMS, respectively. Pollen mass fraction is 60%.
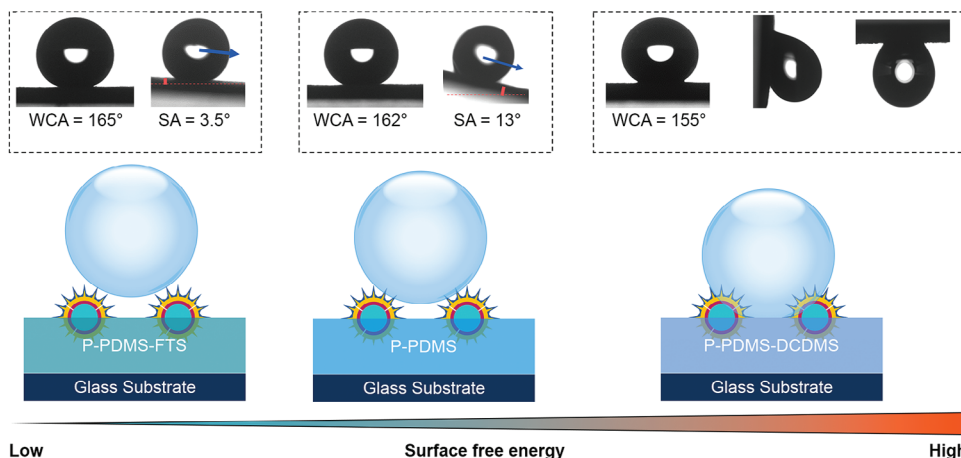
is $\geq$ 50%, the P-PDMS-FTS coating surface exhibits a very low sliding angle of 4.5–8.5° (Video S1, Supporting Information) and contact angle hysteresis of 7–9.5°, indicating a "lotus effect" superhydrophobic surface with minimal water adhesion. This P-PDMS-FTS coating achieves a highest θ_w of 165 $\pm$ 2° and a lowest WSA of 4.5 $\pm$ 1°, resembling the characteristics of lotus leaves (Figure 4J). Similarly, when the pollen content is $\geq$ 50%, the P-PDMS coating surface possesses the highest θ_w of 163 $\pm$ 3°, the lowest WSA of 7.6 $\pm$ 2.6° and CAH of 15.4 $\pm$ 5.8°. Water droplets can run freely in a Petri dish coated with P-PDMS-FTS (Video S2, Supporting Information) and P-PDMS materials. Most superhydrophobic surfaces created by other methods have a WCA between 150° and 160°, with only a few reaching between 160° and 165°, and typically exhibit a WSA of less than 12° (Figure 4J). In comparison, our P-PDMS-FTS and P-PDMS coatings achieved the best WCA while achieving relatively low WSA, respectively. However, P-PDMS-OTS and P-PDMS-DCDMS exhibit a high WSA of more than 30° and can even be suspended at 90° or inverted at 180°, yet they fail to display the "lotus effect" superhydrophobic surfaces, despite having WCAs exceeding 150°.

The relative motion of a water droplet being squeezed, dragged, and subsequently detached on a superhydrophobic surface can be used to assess water adhesion, as illustrated in Figure S7 (Supporting Information). Water droplets can detach from the P-PDMS-FTS surface after being squeezed and dragged (Video S3, Supporting Information), further demonstrating that the P-PDMS-FTS coating is superhydrophobic with low water ad-

hesion. After being squeezed, the water droplets can be dragged but will not detach from the P-PDMS superhydrophobic surface. This indicates that the P-PDMS surface exhibits good superhydrophobicity and relatively low water adhesion, though its water adhesion is slightly higher than that of the P-PDMS-FTS coating. Despite the P-PDMS-OTS and P-PDMS-DCDMS coatings exhibiting a high θ_w of over 150°, they also demonstrate a high WSA. Finally, on P-PDMS-OTS and P-PDMS-DCDMS surfaces, the water droplet could not be dragged after being squeezed indicating that water has high adhesion on these surfaces.

After impacting a surface, droplets may bounce, stick, or spread. The ability of water droplets to bounce on a surface is another important indicator of surface wetting properties and water adhesion to the surface. To further evaluate the adhesion of water to superhydrophobic surfaces, we conducted a water droplet bouncing experiment on various coated surfaces with $f_{pollen} = 60\%$ (**Figure 5**). It was found that the water droplet exhibited four rebounds on the surface of the P-PDMS-FTS coating (Video S4, Supporting Information), only one obviously effective rebound on the P-PDMS surface and weak rebounding on the P-PDMS-OTS surface. Additionally, water droplets failed to rebound and remain adhered to the surface of P-PDMS-DCDMS. These results further emphasize that the P-PDMS-FTS coating exhibits the lowest water adhesion akin to a lotus leaf characterized by a high θ_w and low WSA. In the case of the P-PDMS-FTS coating, water droplets are expected to sit on top of the tips of the sunflower pollen spikes (**Figure 6**). Similarly, the P-PDMS

**ADVANCED
SCIENCE NEWS**

www.advancedsciencenews.com

**NANO · MICRO
small**

www.small-journal.com

Figure 6. Photos of water droplets sitting and sliding on (left) P-PDMS-FTS and (center) P-PDMS surfaces, and sitting, hanging at 90° and hanging upside down at 180° on the (right) P-PDMS-OTS surface. Schematic diagrams illustrate the mechanism of water droplets interacting with surfaces of P-PDMS-FTS, P-PDMS and P-PDMS-DCDMS (or P-PDMS-OTS).

surface also demonstrates low water adhesion, as evidenced by its high θ_w and low WSA, indicating that water droplets are likely to rest on the spikes of the sunflower pollen, although certain portions of the spikes may be submerged within the water droplets (Figure 6). Conversely, the P-PDMS-OTS and P-PDMS-DCDMS surfaces exhibit high water adhesion akin to a rose petal, where water droplets adhere to the surface when it was placed vertically or upside down (Figure 6), despite having a high θ_w. The P-PDMS-OTS and P-PDMS-DCDMS coatings were polymerized at room temperature, as high-temperature treatment would cause the coatings to completely break. Polymerization at room temperature led to incomplete polycondensation of OTS and DCDMS, preventing the formation of a fully developed polysiloxane network after hydrolysis. The partially condensed polysiloxane from OTS and DCDMS contains numerous Si-OH groups, which may explain the higher water adhesion observed on the P-PDMS-OTS and P-PDMS-DCDMS surfaces compared to the P-PDMS surface, despite their similar surface structures and comparable surface free energy. In the case of P-PDMS-OTS and P-PDMS-

DCDMS coatings, the entire sunflower spikes under the water droplet are expected to be embedded in the water droplet (Figure 6). The difference between a "lotus effect" surface with low water adhesion and a "rose petal effect" surface with high water adhesion primarily arises from the variations in their hierarchical micro/nanostructures.[3b,34] However, our above study demonstrates that the water adhesion properties of superhydrophobic surfaces can also be modified by simply changing the surface energy without altering the surface structure.

Through investigations involving WCA, WSA, CAH, and water droplet bouncing, it was proven that P-PDMS and P-PDMS-FTS coatings have a "lotus effect" superhydrophobic surface with minimal water adhesion. Consequently, these surfaces hold promise for self-cleaning applications (**Figure 7A**), different to normal surfaces with high water adhesion (Figure 7B). Here, P-PDMS-FTS coatings with pollen contents ranging from 30% to 80% were evaluated for their self-cleaning ability. The sand was initially deposited on these surfaces before conducting the self-cleaning tests with a tilt angle of 10° (Figure 7C; Video S5,
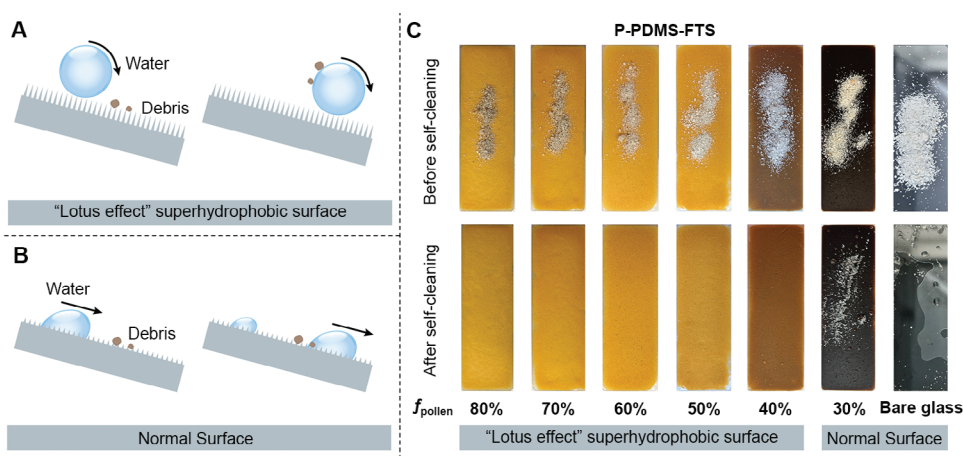
Figure 7. Schematic diagram of (A) the self-cleaning process of a water droplet rolling down on the "lotus effect" superhydrophobic surface and (B) the process of water droplets sliding down on a normal smooth, solid surface. (C) Self-cleaning behavior: Before and after water droplets clean the P-PDMS-FTS superhydrophobic surfaces with sand. Bare glass and P-PDMS-FTS (pollen fraction = 30%) serve as the control surfaces.

Supporting Information). Upon dripping water onto the surfaces, the sand was effectively removed from nearly all surfaces of the P-PDMS-FTS coatings except for the coating containing 30% pollen due to its WCA < 150°. When f_{pollen} = 40%, most of the sand is removed as water droplets roll off. At f_{pollen} = 50–80%, the coating exhibits optimal self-cleaning performance, as all sand are removed when water droplets roll off. On the glass substrate, however, some sand will be washed away with the droplets, while some particles will remain on the surface. These findings demonstrate the self-cleaning capabilities of these "lotus effect" superhydrophobic surfaces attributed to their low water adhesion.

2.3. Water Displacement in Oil Pipeline with Superhydrophobic Inner Surfaces

Most oil/gas pipelines in hilly terrain are typically segmented horizontal, downhill, and uphill sections according to the terrain profile they follow. The gas/oil production and transportation from a reservoir through pipelines may face challenges of liquid (water or hydrates) accumulation in the lower portions of pipelines in hilly terrain.[35] The liquid accumulation may form liquid plugs at the downstream elbow of the pipelines, causing disturbances in flow and instability and internal corrosion of pipelines due to water contact with pipe walls. To prevent corrosion or mitigate its rate, it is crucial to minimize or avoid direct contact between water and the surfaces of the pipes. Here, we propose a strategy to facilitate water displacement in oil pipelines by applying our P-PDMS or P-PDMS-FTS coating to create a superhydrophobic surface on the inner wall of the pipeline. **Figure 8A** shows the water contact angle in mineral oil (θ_{w-o}) for P-PDMS and P-PDMS-FTS surfaces. The P-PDMS coating exhibits a θ_{w-o} of 158–163° when f_{pollen} is 40–80%, while the P-PDMS-FTS coating has a θ_{w-o} of 165–169° when f_{pollen} is 40–70%. Simultaneously, the mineral oil contact angle (OCA) on the P-PDMS-FTS and P-PDMS coatings was measured in air. The P-PDMS-FTS coating exhibited an OCA between 125° and 140° (Figure S8, Supporting Information), whereas mineral oil spreads on P-PDMS, resulting in an OCA close to zero. The interfacial tension between water and mineral oil was measured to be 16.4 ± 1.5 mN m^{-1} and the density of mineral oil is 0.84 g mL^{-1}. The buoyancy of water droplets causes a significant reduction in the apparent gravity of water droplets in mineral oil. This reduction in apparent gravity, coupled with the interfacial tension between water and mineral oil, as well as the "lotus effect" superhydrophobic surface collectively led to an increased θ_{w-o} compared to its corresponding θ_w. Thus, the P-PDMS and P-PDMS-FTS coatings are expected to facilitate water displacement in oil pipelines situated in hilly terrain.

As a demonstration, we applied the superhydrophobic P-PDMS and P-PDMS-FTS coating (with f_{pollen} = 60%) to the inner surfaces of the pipelines. Figure 8B and Figure S9 (Supporting Information) illustrate the schematic diagram and photograph respectively of the experimental setup designed for water displacement in the oil pipeline featuring a superhydrophobic inner surface. The Reynolds number is ≈26.0 in the experiment, based on a flow rate of 290 mL·min^{-1}, a mineral oil density of 0.84 g·mL^{-1}, a viscosity range of 11.89–14.63 cP, and a pipeline inner diameter of 15 mm. In this study, we investigated the potential application of our P-PDMS-FTS and P-PDMS superhy-

drophobic coatings for water displacement in oil pipelines with superhydrophobic inner surfaces, focusing specifically on laminar flow conditions with a low Reynolds number. Oil and water were allowed to flow through bare curved glass pipelines (serving as the control without any coating) with a bending angle of β = 20° (Figure 8C). Notably, red-dyed water always accumulated at the elbows of the curved glass pipelines forming water plugs. As the liquid flowed, the accumulated water consistently clogged at the lower sections of the pipelines as demonstrated in Figures 8C, and Video S6 (Supporting Information). Upon application of the superhydrophobic P-PDMS coating, the water columns within the pipeline can flow smoothly through the curved pipeline following the direction of the liquid flow (Figure 8D; Video S7, Supporting Information). With a bending angle of β = 45° in the curved glass pipeline, water accumulation occurred in the bare glass pipelines (Figure 8E; Video S8, Supporting Information). Remarkably, no water accumulation was also observed at the downstream elbow of the superhydrophobic glass pipeline with β = 45°, as shown in Figure 8F and Video S9 (Supporting Information) (P-PDMS coating), Figure S10 and Video S10 (Supporting Information) (P-PDMS-FTS coating). Experimental observations reveal a sequence of water displacement processes within the pipelines which can be divided into four primary stages: i) The oil–water mixture enters the horizontal section of the hydrophobic pipeline via the transparent PVC hose (the downcomer), ii) displacement of the water moves toward the elbow of the superhydrophobic pipeline and enters the up-comer of the pipeline, iii) complete the water displacement from the horizontal section, iv) complete the water displacement from the entire superhydrophobic pipeline. These findings demonstrate the efficacy of our "lotus effect" superhydrophobic coatings on the inner walls of pipelines for facilitating water displacement from lower sections of oil pipelines in hilly terrains.

3. Conclusion

Micron-sized natural sunflower pollen features nano-sized spikes uniformly distributed on its exine surface. Utilizing this characteristic, superhydrophobic coatings were effectively produced by incorporating spiky sunflower pollen as filler, PDMS polymer as matrix and low surface energy silanes (FTS, OTS, DCDMS) as additive. The superhydrophobic properties of these coatings arise from their micro-nano hierarchical surface structure along with the non-wetting chemistry of PDMS and silanes. As the mass fraction of sunflower pollen in the coating increases, more spike bodies are exposed on the coating surface resulting in an increase in Ra and water contact angle, thereby creating superhydrophobic surfaces. Additionally, it was observed that surface free energy can significantly influence the sliding angle, contact angle hysteresis and water adhesion to the surface. Despite sharing the same surface structure and roughness, a lower surface energy can yield a superhydrophobic surface with a higher contact angle, lower sliding angle, and reduced water adhesion. As a result, coatings such as P-PDMS-FTS and P-PDMS characterized by low surface energy exhibit a "lotus effect" superhydrophobic surface with minimal water adhesion. Conversely, coatings like P-PDMS-OTS and P-PDMS-DCDMS with higher surface energy manifest a "rose petal effect" superhydrophobic surface featuring heightened water adhesion. These distinctions are further
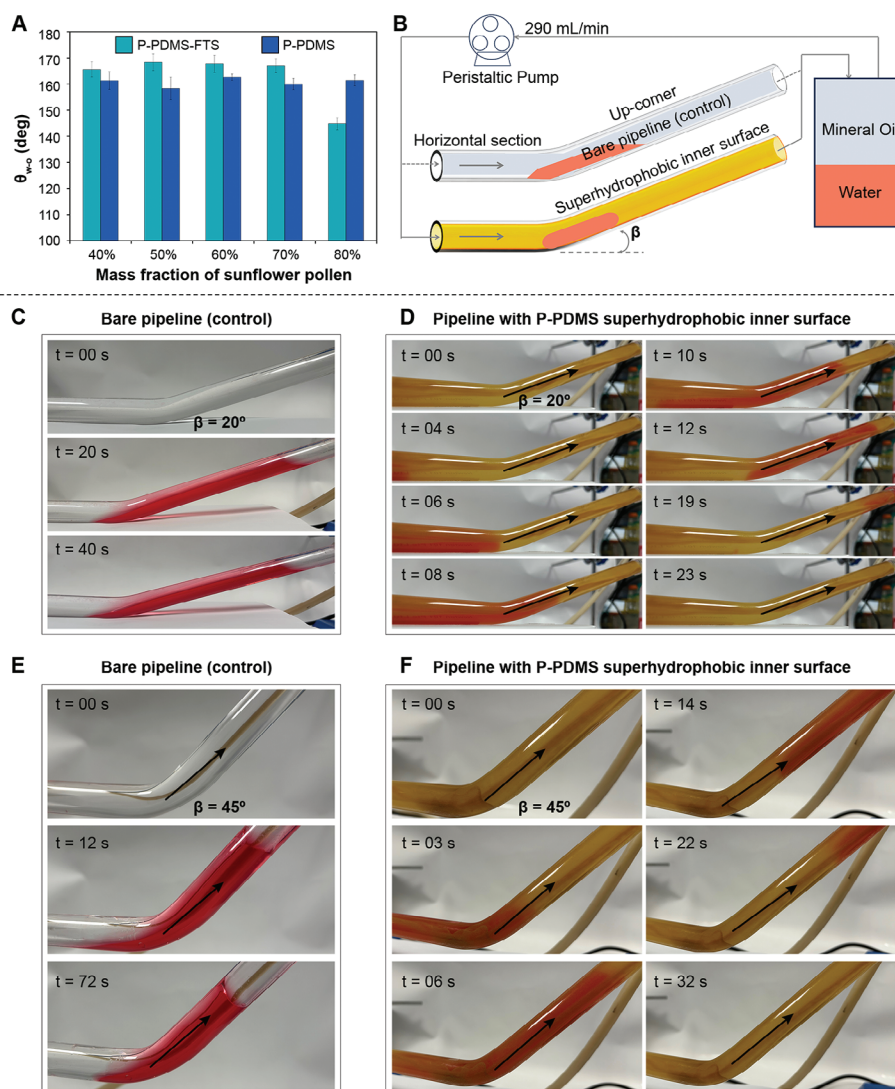
Figure 8. (A) Water contact angles in mineral oil for the P-PDMS and P-PDMS-FTS surfaces ($n = 10$). (B) Schematic diagram of the experimental setup using a bent glass pipeline, which was a bare glass pipeline without any coating (up, control) or a glass pipeline with the superhydrophobic P-PDMS coating (low) on its inner wall for water displacement in the oil pipeline. (C–F) Photographs of flow patterns of mineral oil–water through bent glass pipelines at various time points, including bare pipelines with slopes of (C) 20° and (E) 45° where water resides at the curved and upper sections and bent glass pipelines with slopes of (D) 20° and (F) 45° featuring P-PDMS superhydrophobic coatings on their inner surfaces where water displacement occurs. Mineral oil is a colorless and transparent liquid while the water phase is dyed red.

demonstrated by the water droplet bouncing test performed on these surfaces. Given their "lotus effect" superhydrophobic surfaces with low water adhesion, P-PDMS-FTS and P-PDMS coatings offer self-cleaning capabilities. These coating are particularly suitable for water displacement from lower sections of pipelines in hilly terrain, as demonstrated on laminar flow conditions with a low Reynolds number.

4. Experimental Section

Materials: Bee sunflower pollens were purchased from Xi'an Yuenum Biological Technology Company Ltd., China. A two-component kit of Sylgard 184 silicone elastomer, consisting of Part A (prepolymer) and Part B (curing agent) with a default mixing weight ratio of 10:1, was purchased

from Dow Corning Corporation. OTS (>90%), DCDMS (≥99.5%), and FTS (97%) were purchased from Sigma–Aldrich. Light mineral oil (neat, viscosity: 11.89-14.63 cP, density: 0.84 g·mL^{-1}) and diiodomethane (99%) was also purchased from Sigma–Aldrich. Acetone (Analytical reagents) was obtained from AIK MOH, diethyl ether (Analytical reagents) was obtained from VWR Chemicals and *n*-hexane was purchased from Tedia Company. Pure water was produced by a Milli-Q M device. Sand is natural river sand with typical particle size ranging from tens of microns to 2 mm.

Defatting Sunflower Pollen: The defatting process was previously described by Fan et al.[33] Initially, 500 g of natural bee pollen granules was dispersed in 1 L of deionized water at 50 °C and stirred at 1000 rpm for 2 h using an IKA disperser. The resulting pollen suspension was filtered through a 200 μm nylon mesh to eliminate any impurities and the filtrate was collected. Vacuum filtration was then employed to remove water. Subsequently, the pollen grains were added to 1 L of acetone and stirred at room temperature for 3 h using an IKA disperser (1000 rpm). The acetone

was removed via vacuum filtration and the pollen was washed 3–4 times until the filtrate became clear. After drying, the pollen was dispersed in 1 L of diethyl ether and stirred at room temperature for 2 h to decrease it. This degreasing process was repeated in fresh diethyl ether for an additional 2 h followed by vacuum filtration and washing twice with fresh diethyl ether. The filtered pollen was then dispersed in fresh diethyl ether (1 L) and stirred at room temperature overnight. After removing the ether through vacuum filtration, the degreased pollen was air-dried overnight in a fume hood, then further dried at 50 °C in an oven for one day before being stored for future use.

Preparation of Superhydrophobic Surfaces with Defatted Sunflower Pollen: In 4 mL glass vials, 0.3 g of defatted sunflower pollen was first mixed with PDMS (Sylgard 184 silicone elastomer) precursor (Part A:Part B = 10:1) or a mixture of PDMS precursor (Part A:Part B = 10:1) and one of the silanes (FTS, OTS, DCDMS) with the mass ratio of defatted pollen to PDMS-silane mixture ranging from 3:7 to 8:2 and the mass ratio of PDMS precursor to each silane being 8:2. Following the addition of 2 mL of *n*-hexane into the glass vial and agitation for more than 5 min by Vortex, the suspensions were cast on glass slides and *n*-hexane was allowed to evaporate in a fume hood. Afterward, the dried coatings were left at room temperature for more than 7 days to allow for the curing of PDMS and silane. The resultant cured coatings, comprising sunflower pollen, PDMS, and silane additive (FTS, OTS, DCDMS) designated as P-PDMS, P-PDMS-FTS, P-PDMS-OTS, and P-PDMS-DCDMS were subsequently stored for characterization and future applications.

Surface Characterization: SEM images were taken using a JEOL JSM-7600F Schottky field-emission scanning electron microscope under an acceleration voltage of 5 kV, and samples were sputter-coated with gold for 60 s. The surface morphology, surface roughness Arithmetical mean height in definition area, *Ra*) and thickness of the coatings were measured on a Keyence VHX-7000 digital microscope. Digital Microscopy can capture a depth composition image with the topography of the whole area of the surface under test (magnification: ×1000, vertical pitch: 1 μm), from which roughness information can be obtained with the built-in software. XPS measurements were recorded on a XPS Kratos AXIS Supra with a monochromatic Al Kα x-ray source. FTIR was conducted using a Perkin Elmer Frontier FTIR spectrometer. The absorbance spectra were measured from 400 to 4000 cm^{-1}, with a spectral resolution of 1 cm^{-1} and 32 scans performed.

The WCA was measured using a contact angle meter (Attension Theta Flex C201, Biolin Scientific) via the sessile drop method with a 5 μL water drop placed onto the surface. The measurements were automatically taken by the software's automatic baseline mode and a Young–Laplace fitting model. Five measurements per sample were taken at random locations on the coatings. The CAH was determined as the difference between advancing and receding contact angles, assessed by adding and withdrawing water from the droplet volume of 6 μL. The WSA on superhydrophobic surfaces was determined using a 10 μL water droplet on a Bosch GAM 220 MF Digital Angle Finder. The base leg of the Digital Angle Finder was positioned horizontally, while the fold-out leg, with a superhydrophobic substrate attached to its surface, was manually and slowly adjusted to measure the sliding angle of the droplet on the superhydrophobic surface, as shown in Figure S11 (Supporting Information). When the water droplet began to roll, the adjustment of the fold-out leg was immediately stopped, and the WSA displayed on the Digital Angle Finder was recorded. Bouncing of 6 μL water droplets were tested to evaluate the adhesion of water to the surface and recorded on the contact angle meter, where the distance between the superhydrophobic coating surface and the tip of the needle is ≈7 mm. The relative motion of a water droplet (5 μL) being squeezed, dragged, and subsequently detached on a superhydrophobic surface was also recorded on the contact angle meter, which was also used to evaluate the adhesion of water to the surface.

The P-PDMS and P-PDMS-FTS superhydrophobic substrates were placed into a mineral oil bath. Their water contact angles in mineral oil were measured using the sessile drop method, with a 10 μL water droplet placed onto the surface. The water contact angles of P-PDMS and P-PDMS-FTS surfaces measured in mineral oil were designated as θ_{w-o}. The OCA on the P-PDMS-FTS and P-PDMS coatings was also measured in air using the sessile drop method.

Interfacial Tension Between Water and Mineral Oil: The interfacial tension between water and mineral oil was using the contact angle meter (Attention Theta Flex C201) by the pendant drop method, where a 5 μL drop of water is formed at the end of the needle in mineral oil.

Surface Free Energy: The surface free energy of pure PDMS, PDMS-FTS (PDMS mass fraction = 80%), PDMS-OTS (PDMS mass fraction = 80%) and PDMS-DCDMS (PDMS mass fraction = 80%) films without pollen (pollen mass fraction = 0%) was calculated with the Owens, Wendt, Rabel and Kaelble (OWRK) method through measuring the static contact angle of water and diiodomethane droplets using the sessile drop method.[36] The OWRK method selects two liquids with known dispersive and polar components to measure surface free energy. One liquid with the dominant polar component and another dispersive liquid should be chosen. In this study, water was used as the polar liquid and diiodomethane as the dispersive liquid.

Self-Cleaning Ability: To test the self-cleaning properties of the P-PDMS-FTS surfaces, we used solid foulants such as river sand dispersed on the surface, with a bare glass slide serving as a control. The slides were tilted to ≈10°, and water was dropped onto their surfaces to assess their self-cleaning ability. This process was recorded using a mobile phone camera. The self-cleaning capability was evaluated by observing the residual impurities left on the surfaces.

Water Displacement in Oil Pipeline with Superhydrophobic Inner Surface: The experimental setup utilized in this study simulates possible flow conditions encountered in the lower segments of natural gas and oil pipelines situated in hilly terrain serving to purge accumulated water.[35] The test section in the flow facility consists of three replaceable sub-sections: a transparent PVC hose, a curved glass tube comprising a 200 mm horizontal section and a 220 mm upward inclined section (up-comer), and another PVC hose, all with an inner diameter of 15 mm. The inner wall of the curved glass tube was coated with a superhydrophobic P-PDMS (or P-PDMS-FTS) coating, with a pollen mass fraction of 60%. A mixture of mineral oil and water was drawn from their interface in the tank (storage bottle) using a peristaltic pump, flowing into the curved glass pipeline at a rate of 290 mL·min^{-1}. The flow patterns within the curved glass pipeline were recorded at different time points using a smartphone camera.

Supporting Information

Supporting Information is available from the Wiley Online Library or from the author.

Acknowledgements

Conflict of Interest

The authors declare no conflict of interest.

Data Availability Statement

Research data are not shared.

Keywords

**ADVANCED
SCIENCE NEWS**

www.advancedsciencenews.com

**NANO · MICRO
small**

www.small-journal.com

[1] W. Barthlott, C. Neinhuis, *Planta* **1997**, *202*, 1.

[2] C. Neinhuis, W. Barthlott, *Ann. Bot.* **1997**, *79*, 667.

[3] a) L. Feng, Y. Zhang, J. Xi, Y. Zhu, N. Wang, F. Xia, L. Jiang, *Langmuir* **2008**, *24*, 4114; b) B. Bhushan, E. K. Her, *Langmuir* **2010**, *26*, 8207.

[4] a) M. J. Liu, S. T. Wang, L. Jiang, *Nat. Rev. Mater.* **2017**, *2*, 17036; b) T. Sun, L. Feng, X. Gao, L. Jiang, *Acc. Chem. Res.* **2005**, *38*, 644.

[5] a) A. G. Leão, B. G. Soares, A. A. Silva, E. C. L. Pereira, L. F. C. Souto, A. C. Ribeiro, *Surf. Coat. Technol.* **2023**, *462*, 129479; b) H. Li, J. Lai, M. Yao, Y. M. Leng, Z. D. Wu, J. Zhang, H. L. Peng, Z. M. Qiu, *Appl. Surf. Sci.* **2022**, *601*, 154109; c) S. K. Sethi, S. Kadian, R. Gogoi, G. Manik, *Surf. Interfaces* **2023**, *37*, 102752; d) F. Q. Li, Y. Liu, H. G. Zhou, G. Z. Tian, *Biomimetics* **2022**, *7*, 132.

[6] B. Zhang, W. Xu, Q. Zhu, Y. Li, B. Hou, *J. Colloid Interface Sci.* **2018**, *532*, 201.

[7] a) K. Yan, F. Zhao, L. Pan, Y. Jiang, Y. Shi, G. Yu, *Nat. Sustainability* **2023**, *6*, 1654; b) Z. Liu, J. Yang, J. Jing, X. Zhang, Y. Fu, M. Li, R. Yuan, H. Wang, *J. Mater. Chem. A* **2023**, *11*, 18081; c) Y. Ye, T. Li, Y. Zhao, J. Liu, D. Lu, J. Wang, K. Wang, Y. Zhang, J. Ma, E. Drioli, X. Cheng, *Sep. Purif. Technol.* **2023**, *317*, 123885.

[8] B. Rezaee, M. Mahlouji Taheri, H. Pakzad, M. Fakhri, A. Moosavi, M. Aryanpour, *Langmuir* **2023**, *39*, 8354.

[9] Z. Han, X. Feng, Z. Jiao, Z. Wang, J. Zhang, J. Zhao, S. Niu, L. Ren, *RSC Adv.* **2018**, *8*, 26497.

[10] a) J. Jiang, Y. Shen, Y. Xu, Z. Wang, J. Tao, S. Liu, W. Liu, H. Chen, *Nat. Commun.* **2024**, *15*, 777; b) H. Lambley, G. Graeber, R. Vogt, L. C. Gaugler, E. Baumann, T. M. Schutzius, D. Poulikakos, *Nat. Phys.* **2023**, *19*, 649; c) H. He, W. Huang, Z. G. Guo, *Mater. Today Phys.* **2023**, *30*, 100927; d) Y. Zhao, C. Yan, T. Hou, H. Dou, H. Shen, *ACS Appl. Mater. Interfaces* **2022**, *14*, 26077.

[11] a) Q. Chen, C. Zhang, Y. Cai, X. Luo, B. Wang, Q. Song, Z. Liu, *Appl. Surf. Sci.* **2023**, *615*, 156403; b) L. Xin, H. Li, J. Gao, Z. Wang, K. Zhou, S. Yu, *Friction* **2023**, *11*, 716.

[12] a) D. Yue, X. Jiang, H. Yu, D. Sun, *Chem. Eng. J.* **2023**, *463*, 142389; b) J. Wang, S. Lee, A. R. Bielinski, K. A. Meyer, A. Dhyani, A. M. Ortiz-Ortiz, A. Tuteja, N. P. Dasgupta, *Adv. Mater. Interfaces* **2020**, *7*, 2000672; c) S. Tang, Z. Wu, G. Feng, L. Wei, J. Weng, E. Ruiz-Hitzky, X. Wang, *Chem. Eng. J.* **2023**, *454*, 140457.

[13] a) J. Lou, Y. Zhao, Y. Meng, J. Su, J. Han, *Synth. Met.* **2023**, *293*, 117293; b) D. Zhang, R. Xu, S. Chen, H. Du, S. Qian, F. Peng, X. Liu, *Bioact. Mater.* **2023**, *30*, 15; c) L.-H. Zhang, J.-L. Yang, Y.-Y. Song, Y. Liu, Z.-Q. Zhang, *Langmuir* **2023**, *39*, 8379.

[14] a) Z. Liu, C. Zhang, J. Jing, X. Zhang, C. Wang, F. Liu, M. Jiang, H. Wang, *Chem. Eng. J.* **2022**, *436*, 135273; b) W. Tang, Y. Jian, M. Shao, Y. Cheng, J. Liu, Y. Liu, D. W. Hess, H. Wan, L. Xie, *Colloids Surf., A* **2023**, *666*, 131314; c) M. Y. Qiao, G. J. Ji, Y. Lu, B. B. Zhang, *J. Ind. Eng. Chem.* **2023**, *121*, 215; d) C. B. Hu, K. Kwan, X. Y. Xie, C. G. Zhou, K. N. Ren, *React. Funct. Polym.* **2022**, *179*, 105381; e) M. E. Mohamed, O. Adel, E. Khamis, *Sci. Rep.* **2023**, *13*, 9453; f) H. Li, Y. He, P. Luo, H. Zhou, B. Liu, Y. He, R. Song, Z. Zhang, Y. Fan, *Surf. Coat. Technol.* **2022**, *450*, 129008; g) C. Bai, C. Hu, X. Zhang, W. Zhang, B. Ma, T. Li, *Colloids Surf., A* **2022**, *651*, 129635.

[15] C. Xu, M. Gao, X. Yu, J. Zhang, Y. Cheng, M. Zhu, *Nanomicro. Lett.* **2023**, *15*, 64.

[16] a) C. Yang, Q. Zeng, J. Huang, Z. Guo, *Adv. Colloid Interface Sci.* **2022**, *306*, 102724; b) R. N. Wenzel, *J. Phys. Colloid Chem.* **1949**, *53*, 1466; c) A. B. D. Cassie, S. Baxter, *Trans. Faraday Soc.* **1944**, *40*, 546.

[17] T. Nishino, M. Meguro, K. Nakamae, M. Matsushita, Y. Ueda, *Langmuir* **1999**, *15*, 4321.

[18] a) A. Lafuma, D. Quéré, *Nat. Mater.* **2003**, *2*, 457; b) D. Wang, Q. Sun, M. J. Hokkanen, C. Zhang, F.-Y. Lin, Q. Liu, S.-P. Zhu, T. Zhou, Q. Chang, B. He, Q. Zhou, L. Chen, Z. Wang, R. H. A. Ras, X. Deng, *Nature* **2020**, *582*, 55.

[19] H. J. Ensikat, P. Ditsche-Kuru, C. Neinhuis, W. Barthlott, *Beilstein J. Nanotechnol.* **2011**, *2*, 152.

[20] J. H. Park, M. Namvari, G. M. Choi, J. Rahmannezhad, H. J. Jeong, M. C. Hong, C. M. Lee, S. M. Noh, S. G. Kim, S.-C. Yang, H. S. Lee, *Langmuir* **2023**, *39*, 4622.

[21] L. Gong, W. Yang, Y. Sun, C. Zhou, F. Wu, H. Zeng, *Adv. Funct. Mater.* **2023**, *33*, 2214947.

[22] a) J. J. Kalmoni, F. L. Heale, C. S. Blackman, I. P. Parkin, C. J. Carmalt, *Langmuir* **2023**, *39*, 7731; b) X. Huang, M. Sun, X. Shi, J. Shao, M. Jin, W. Liu, R. Zhang, S. Huang, Y. Ye, *Chem. Eng. J.* **2023**, *454*, 139981.

[23] R. Alimohammadzadeh, I. Sanhueza, A. Cordova, *Sci. Rep.* **2023**, *13*, 3157.

[24] P. Kothary, X. Dou, Y. Fang, Z. Gu, S.-Y. Leo, P. Jiang, *J. Colloid Interface Sci.* **2017**, *487*, 484.

[25] G. He, M. Wan, Z. Wang, Y. Zhao, L. Sun, *Colloids Surf., A* **2023**, *662*, 130962.

[26] M. Ghasemlou, P. H. Le, F. Daver, B. J. Murdoch, E. P. Ivanova, B. Adhikari, *ACS Appl. Mater. Interfaces* **2021**, *13*, 36558.

[27] N.-J. Cho, *Mater. Today* **2022**, *61*, 1.

[28] a) R. C. Mundargi, M. G. Potroz, S. Park, H. Shirahama, J. H. Lee, J. Seo, N. J. Cho, *Small* **2016**, *12*, 1167; b) T. Maric, M. Z. M. Nasir, N. F. Rosli, M. Budanović, R. D. Webster, N.-J. Cho, M. Pumera, *Adv. Funct. Mater.* **2020**, *30*, 2000112; c) Z. Zhao, J. Deng, H. Tae, M. S. Ibrahim, S. Suresh, N.-J. Cho, *Adv. Mater.* **2022**, *34*, 2109367.

[29] a) C. C. Hou, W. J. Wang, Y. Zhang, Z. S. Guan, *Appl. Surf. Sci.* **2012**, *258*, 6864; b) E. Bormashenko, T. Stein, R. Pogreb, D. Aurbach, *J. Phys. Chem. C* **2009**, *113*, 5568.

[30] a) D. S. Zhao, Y. W. Li, Z. D. Zhang, T. Xu, C. Ye, T. Q. Shi, Y. T. Wang, *Mater. Horiz.* **2023**, *10*, 1121; b) R. W. Weber, *Ann. Allergy, Asthma, Immunol.* **1998**, *80*, 141.

[31] R. C. Mundargi, M. G. Potroz, J. H. Park, J. Seo, J. H. Lee, N. J. Cho, *RSC Adv.* **2016**, *6*, 16533.

[32] Y. Hwang, M. S. B. Ibrahim, J. Deng, J. A. Jackman, N.-J. Cho, *Adv. Funct. Mater.* **2021**, *31*, 2101091.

[33] T. F. Fan, S. Park, Q. Shi, X. Y. Zhang, Q. M. Liu, Y. Song, H. Chin, M. S. Bin Ibrahim, N. Mokrzecka, Y. Yang, H. Li, J. H. Song, S. Suresh, N. J. Cho, *Nat. Commun.* **2020**, *11*, 1.

[34] C. Chen, M. M. Liu, L. P. Zhang, Y. Y. Hou, M. N. Yu, S. H. Fu, *ACS Appl. Mater. Interfaces* **2019**, *11*, 7431.

[35] a) X. Song, Y. Yang, T. Zhang, K. Xiong, Z. Wang, *J. Pet. Sci. Eng.* **2017**, *157*, 780; b) E. Hamami Bissor, A. Ullmann, N. Brauner, *J. Nat. Gas Sci. Eng.* **2020**, *73*, 103046.

[36] a) F. M. Fowkes, *Ind. Eng. Chem.* **1964**, *56*, 40; b) D. K. Owens, R. C. Wendt, *J. Appl. Polym. Sci.* **1969**, *13*, 1741.

[37] a) X. Zhang, Z. Liu, Y. Li, C. Wang, Y. Zhu, H. Wang, J. Wang, *Chem. Eng. J.* **2019**, *371*, 276; b) J. Shang, Y. Jiang, W. Wang, *Polymers* **2022**, *14*, 3124; c) R. n. R. Hashjin, Z. Ranjbar, H. Yari, G. Momen, *Surf. Interfaces* **2022**, *33*, 102282; d) Y. Hu, X. Ma, H. Bi, J. Sun, *Colloids Surf., A* **2020**, *603*, 125227; e) M. R. Ghadimi, A. Dolati, *Prog. Org. Coat.* **2020**, *138*, 105388; f) X. Li, H. Yin, Y. Cao, L. Hu, X. Lin, C. Hu, *Ceram. Int.* **2023**, *49*, 19786; g) K. Vidal, E. Gómez, A. M. Goitandia, A. Angulo-Ibáñez, E. Aranzabe, *Coatings* **2019**, *9*, 627.

[38] a) X. Zhang, Z. Wang, S. Liu, J. Chen, W. Zhang, F. Hu, *J. Sol–Gel Sci. Technol.* **2023**, *108*, 73; b) S. Luan, P. Xu, Y. Zhang, L. Xue, Y. Song, C. Gui, *ACS Appl. Mater. Interfaces* **2022**, *14*, 53433; c) L. Dong, Z. Zhang, R. Ding, L. Wang, M. Liu, Z. Weng, Z. Wang, D. Li, *Surf. Coat. Technol.* **2019**, *372*, 434; d) X. Li, G. Zhang, X. Xu, G. Zhao, Y. Liu, S. Yin, *Ceram. Int.* **2023**, *49*, 26338.

[39] A. Ahmad, H. Albargi, M. Ali, M. Batool, A. Nazir, M. B. Qadir, Z. Khaliq, S. N. Arshad, F. A. Harraz, *J. Sci.: Adv. Mater. Devices* **2023**, *8*, 100536.

[40] a) H. Yang, Y. Gao, G. S. Frankel, W. Qin, T. Li, Z. Huang, L. Wu, *Appl. Surf. Sci.* **2020**, *499*, 143916; b) H. Peng, Z. Luo, L. Li, Z. Xia, J. Du, B. Zheng, *Mater. Res. Express* **2019**, *6*, 096586; c) J. Satyarathi, V. Kumar,

S. Kango, R. Verma, N. Sharma, R. Gupta, *Surf. Topogr.: Metrol. Prop.* **2022**, *10*, 045017; d) Y. Jian, H. Gao, Y. Yan, *Surf. Interfaces* **2022**, *34*, 102353.

[41] a) M. Liu, X. Tan, X. Li, J. Geng, M. Han, K. Wei, X. Chen, *Colloids Surf., A* **2023**, *658*, 130624; b) X.-J. Guo, D. Zhang, C.-H. Xue, B.-Y. Liu, M.-C. Huang, H.-D. Wang, X. Wang, F.-Q. Deng, Y.-P. Pu, Q.-F. An, *ACS Appl. Mater. Interfaces* **2023**, *15*, 4612; c) Y. Sun, H. Zhao, H. Mao, M. Duan, K. Wang, N. Bao, Z.-P. Zhao, H. Li, *Sep. Purif. Technol.* **2023**, *304*, 122041.

[42] a) D. Ding, Q. Wu, J. Wang, Y. Chen, Q. Li, L. Hou, L. Zhao, Y.-Y. Xu, *Compos. Commun.* **2023**, *38*, 101509; b) C. Shao, M. Jiang,

J. Zhang, Q. Zhang, L. Han, Y. Wu, *Appl. Surf. Sci.* **2023**, *609*, 155259; c) C. H. Xue, M. M. Du, X. J. Guo, B. Y. Liu, R. X. Wei, H. G. Li, M. C. Huang, F. Q. Deng, S. T. Jia, *Cellulose* **2021**, *28*, 5107.

[43] K. Xu, W. Shen, S. Yang, Y. Wu, D. Zhao, Z. Leng, Y. Tang, H. Zhu, S. Liu, Z. Zhang, *Colloids Surf., A* **2023**, *657*, 130507.

[44] a) B. Mockenhaupt, H. J. Ensikat, M. Spaeth, W. Barthlott, *Langmuir* **2008**, *24*, 13591; b) M. Yamamoto, N. Nishikawa, H. Mayama, Y. Nonomura, S. Yokojima, S. Nakamura, K. Uchida, *Langmuir* **2015**, *31*, 7355.